Numerical prediction of enhanced heat flux due to shock-on-shock interaction in hypersonic nonequilibrium flow

Min G. Lee
Center for Simulation of Advanced Rockets, University of Illinois at Urbana-Champaign, USA

Keywords *Flow, Hypersonic, Thermochemical*

Abstract *This paper describes the numerical solutions of type-IV shock-on-shock interactions in hypersonic thermochemical nonequilibrium air flows around blunt bodies. The Navier-Stokes equation solver for a chemically reacting and vibrationally relaxing gas mixture was applied to the present problem, where the concepts of the Advection Upstream Splitting Method (AUSM) and the Lower-Upper Symmetric Gauss-Seidel (LU-SGS) method were basically employed along with the two-temperature thermochemical model of Park. The aerodynamic heating with or without the shock-on-shock interaction to a sphere and circular cylinders are simulated for a hypersonic nonequilibrium flow. The numerical results show that typical type-IV shock-on-shock interaction pattern with a supersonic jet structure is also formed in a high-enthalpy thermochemical nonequilibrium flow, and that the contribution of convective heat flux in the translational/rotational mode to the total heat flux is dominant. Furthermore, the inherent unsteadiness of nonequilibrium type-IV shock-on-shock interaction flowfield is discussed briefly.*

Introduction

The evaluation of aerodynamic heating load during hypersonic flight has been one of the key issues in the design of hypersonic vehicles. Especially, shock-on-shock interference heating phenomena is an important and critical problem in the development of air-breathing hypersonic vehicles. It is well known that the shock-on-shock interference heating extremely enhances local pressure and heat transfer rate on the vehicle body, which leads to serious damage of part of the body. A detailed flowfield structure is required to predict the magnitude of the aerodynamic heating rate in such a flowfield. Many researchers, therefore, have investigated the shock-on-shock interference heating during the past decades, both experimentally and numerically.

Edney (1968) classified the hypersonic shock-on-shock interaction flowfield into six major patterns and measured distributions of pressure and heat transfer rate on aerodynamic body surface. It was shown that the interaction pattern is strongly dependent on the location where the oblique impinging shock intersects with the bow shock wave. The most serious interaction pattern of interest is the so-called type-IV interaction that involves a supersonic jet

International Journal of Numerical Methods for Heat & Fluid Flow, Vol. 9 No. 2, 1999, pp. 114-135,

structure impinging nearly normal to the body surface. This supersonic impinging jet between shear layers developing from two triple points on the bow shock system generates a local stagnation region of high pressure and of high heating rate (see Figure 1). The type-IV shock-on-shock interaction occurs when an oblique shock wave impinges in the lower region than the upper sonic line of simple blunt body flowfield without an impinging shock. Recent experiment by Holden *et al.* (1992) indicated that the local peak heat transfer rate due to the type-IV shock-on-shock interaction could be increased up to 32 times the stagnation point value without an impinging shock.

A number of numerical studies on shock-on-shock interference heating problems have been conducted since the work of Tannehill *et al.* (1976). Recent numerical studies include Klopfer and Yee (1988), Lind (1997), Zhong (1994), Thareja *et al.* (1989), and Gaitonde and Shang (1995), etc. Most of these numerical studies, however, assume a perfect gas model in high Mach number free-streams. The supersonic jet embedded in the type-IV interaction flowfield has the high-energy stream and the gas temperature behind a jet bow shock is considerably increased. It is well known that the high temperature results in

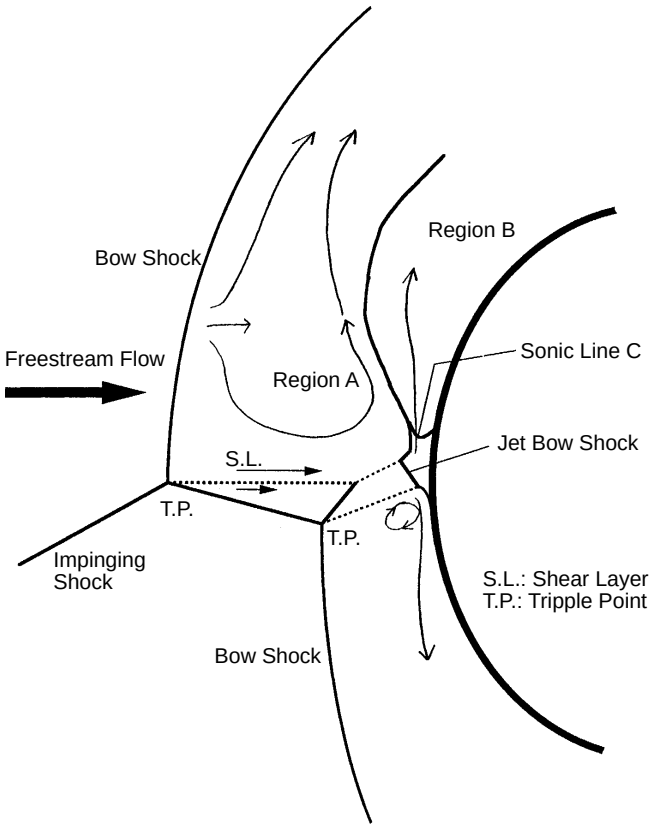

Figure 1.
Typical flowfield structure of type-IV shock-on-shock interaction

non-ideal thermodynamic behavior of gas, and that the thermochemical relaxation phenomena behind a strong shock greatly affects the aerodynamic heating in a high enthalpy flow. It is, therefore, necessary to account for high temperature effects such as chemical reaction and excitation of internal energy modes in numerical modeling of hypersonic shock-on-shock interaction heating. Kortz *et al.* (1995) reported experimental results on the conditions leading to a significant dissociation of nitrogen molecules behind a strong bow shock wave by using a high enthalpy shock tunnel with a free-piston driver. Carlson and Wilmoth (1994) used a direct simulation Monte Carlo (DSMC) technique in conjunction with nonequilibrium air chemistry to compute the type-IV interference heating flow in a continuum flow regime. Also Bruck (1997) computed the nonequilibrium type-IV shock interaction at free flight conditions by using an implicit finite difference scheme for the thin layer Navier-Stokes equations.

In this study, we present the numerical solution of hypersonic type-IV shock-on-shock interaction field in nonequilibrium air flows around blunt body with the purpose of predicting convective heat transfer rates to the body surfaces. The present numerical study employs the two-temperature thermochemical model of Park (1989) and the finite-rate dissociation/recombination air chemistry. The air chemistry model consists of five neutral species for the description of thermochemical nonequilibrium processes in high temperature air. Hence, we solve the full Navier-Stokes equations for a multi-component reacting and vibrationally relaxing gas mixture. Inviscid convective terms of the governing equations are discretized with Advection Upwind Splitting Method (AUSM) (Liou and Steffen, 1993), while viscous fluxes are approximated with a standard second-order centered scheme. The Lower-Upper Symmetric Gauss-Seidel (LU-SGS) method by Yoon and Jameson (1988) is adopted effectively to integrate the governing equations with stiff source terms, where approximate linearization is made for inviscid and viscous fluxes, and exact linearization for thermochemical source terms.

The present method is first applied to analyze viscous hypersonic nonequilibrium flows around a blunt body experimented in hypersonic impulse facilities for the purpose of code validation. The calculation simulate the results of those experiments in detail, where convective heat flux distributions over a sphere surface were measured under various free-stream values of enthalpy ranging from 10 to 20 MJ/kg and optical flow visualizations were conducted. The hypersonic type-IV shock-on-shock interaction phenomena, then, are calculated using the present code. In order to study the thermochemical nonequilibrium effects in such a complicated high-enthalpy interaction flow, detailed flowfield analysis is performed numerically.

Governing equations

We assume that the high-temperature air under consideration is composed of five neutral species (N, O, NO, N_2 and O_2) and the two internal energy modes describing thermal nonequilibrium are characterized by the translational/

rotational temperature T and the vibrational/electronic temperature T_v, respectively. The modeling equations, therefore, are mass conservation equations for each chemical species, momentum equations, a vibrational/ electronic energy conservation equation, and a total energy conservation equation. The governing equations written in Cartesian coordinates are

$$\partial_t \mathbf{Q} + \partial_m \mathbf{f}_m = \partial_m \mathbf{g}_m + \mathbf{H} \tag{1}$$

where the solution vector $\mathbf{Q}$, the inviscid and viscous flux vectors $\mathbf{f}_k$ and $\mathbf{g}_k$ (k=1, 2, 3) and the thermochemical source term $\mathbf{H}$, are given by

$$\begin{aligned}
&\mathbf{Q} = [\rho_1, \cdots, \rho_N, \rho u_1, \rho u_2, \rho u_3, E_v, E]^T, \\
&\mathbf{f}_k = [\rho_1 u_k, \cdots, \rho_N u_k, \rho u_1 u_k + \delta_{1k} p, \rho u_2 u_k + \delta_{2k} p, \rho u_3 u_k + \\
&\qquad \delta_{3k} p, E_v u_k, (E+p) u_k]^T, \\
&\mathbf{g}_k = [J_{1,k}, \cdots, J_{N,k}, \tau_{1,k}, \tau_{2,k}, \tau_{3,k}, q_{v,k} + h_{v,s} J_{s,k}, q_k + h_s J_{s,k} + u_m \tau_{m,k}]^T, \\
&\mathbf{H} = [\dot{\omega}_1, \cdots, \dot{\omega}_N, 0, 0, 0, \dot{\omega}_v, 0]^T
\end{aligned} \tag{2}$$

In these equations ∂ means partial derivative with respect to time or space coordinates, ρ denotes the density, u is the velocity, E is the energy per unit mass, p is the pressure, δ is the Kronecker's delta, h is the enthalpy, J is the mass flux due to diffusion, τ is the stress tensor, q is the heat flux, ω_N is the mass source of species, and ω_v is the vibrational/electronic energy source. In super/subscripts, s denotes the chemical species (s=1,...,N), v the vibrational/ electronic mode, T the transposition, N the number of species. The summation on repeating index s, and on repeating index m (from 1 to 3) is assumed in the above equations.

Equations (1) and (2) are closed by the following thermodynamic relations:

$$\begin{aligned}
&E_t = 0.5 \rho u_m u_u + \sum_{s=1}^{N} \rho_s (e_{tr,s} + e_{vib,s} + e_{el,s} + e_{o,s}), \\
&E_v = \sum_{s=molecule} \rho_s (e_{vib,s} + e_{el,s}), \\
&e_{tr,s} = c_{v,s} R_s T, \\
&h_s = (1 + c_{v,s}) R_s T + (e'_{vib,s} + e'_{el,s}) T_v + e_{o,s} \\
&h_{v,s} = (e'_{vib,s} + e'_{el,s}) T_v, \\
&p = \sum_{s=1}^{N} \rho_s R_s T
\end{aligned} \tag{3}$$

where e, T and R_s denote the internal energy per unit mass, the temperature and the gas constant of species s, respectively. The prime $(\,)'$ means derivative with respect to the vibrational temperature T_v. The stress tensor $\tau_{i,j}$, total and vibrational heat flux vectors, q_k and $q_{v,k,}$ and mass flux vector $J_{v,k}$ are given by

$$\tau_{i,j} = \mu(\partial_i u_j + \partial_j u_i) - (2/3)\mu\partial_m u_m \delta_{i,j},$$
$$q_k = \eta\partial_k T + \eta_v \partial_k T_v,$$
$$q_{v,k} = \eta_v \partial_k T_v, \quad (4)$$
$$J_{v,k} = \rho D_s \partial_k y_s$$

where y_s is the mole fraction of each chemical species, μ is the mixture viscosity, η and η_v are the frozen and vibrational thermal conductivity, and D_s is the effective diffusion coefficient of species s.

Nonequilibrium chemistry model

The five species dissociation/recombination model of a high-temperature air is used in all of the calculations. The model is defined when a set of *Nr* chemical reactions and appropriate expressions for the forward/backward rate coefficients are provided. Consider the two-temperature thermochemical model of Park (1989) that accounts for a coupling between the finite-rate vibrational and chemical processes by a single rate-controlling temperature T_a, which is defined as $T_a = \sqrt{T \cdot T_v}$. The chemical reactions considered in the present calculation are those of thermal dissociation of molecules and recombination expressed as

$$\mathrm{N_2+M \leftrightarrow N+N+M},$$
$$\mathrm{NO+M \leftrightarrow N+O+M}, \quad (4a)$$
$$\mathrm{O_2+M \leftrightarrow O+O+M}$$

and the exchange reactions involving NO, or Zeldovich reactions

$$\mathrm{N_2+O \leftrightarrow NO+N},$$
$$\mathrm{NO+M \leftrightarrow O_2+N} \quad (4b)$$

where M is a collision partner or catalytic molecule; it can be any one of the five species (i.e., M=N, O, NO, N_2 and O_2). Seventeen elementary reactions (15 dissociation/recombination and two exchange reactions) are represented by the above chemical reaction scheme.

The components of the thermochemical source vector **H** in equations (1) and (2) are defined in the following way. The mass rate of production of species s per unit volume is expressed as

$$\dot{\omega}_s = M_s \sum_{r=1}^{Nr} (b_{s,r} - f_{s,r})(R_r^f - R_r^b),$$
$$R_r^f = k_r^f \prod_s \left(\frac{\rho_s}{M_s}\right)^{f_{s,r}}, \quad (5)$$
$$R_r^b = k_r^b \prod_s \left(\frac{\rho_s}{M_s}\right)^{b_{s,r}}$$

where Nr is the number of the chemical reactions, $f_{s,r}$ and $b_{s,r}$ are the stoichiometric coefficients for species s in the forward and backward r-th reaction, respectively, and k_r^f and k_r^b are the forward and backward r-th reaction rate coefficients, respectively.

The forward/backward reaction rate coefficients are assumed to be functions of the rate-controlling temperature T_a and described by the modified forms of Arrhenius equation as follows:

$$k_r^f = A_r^f (T_a)^{n_r^f} \exp(-E_r^f / kT_a),$$
$$k_r^b = k_r^f / K_r^{eq}(T_a) \tag{6}$$

where k is Boltzmann's constant, and a curve fit of the form proposed by Park (1989) is employed for the equilibrium constant in the r-th reaction, K_r^{eq}. The expression takes the form

$$K_r^{eq} = \exp(B_r^1 + B_r^2 \ln Z + B_r^3 Z + B_r^4 Z^2 + B_r^5 Z^3),$$
$$Z = 10^4 / T \tag{7}$$

where the values of the parameters A_r^f and n_r^f, and the constant are taken from the data set compiled by Park (1989).

Vibrational relaxation model

The vibrational/electronic energy source term, modeled according to the theory developed by Landau and Teller (Vincenti and Kruger, 1993), accounts for the finite-rate relaxation of vibrational/electronic energy due to collisions between heavy particles, and the addition or removal of vibrational/electronic energy due to endothermic chemical reactions. It can be expressed as follows:

$$\dot{\omega}_v = \sum_{s=molecule} \rho_s \frac{e_{vib,s}(T) - e_{vib,s}(T_v)}{\tau_s} + \sum_{s=molecule} [e_{vib,s}(T_v) + e_{el,s}(T_v)]\dot{\omega}_s,$$
$$\tau_s = \left(\sum_r \frac{y_r}{\tau_{s,r}}\right)^{-1} \tag{8}$$

where $\tau_{s,r}$ is the characteristic relaxation time of species s in a bath of species r, and calculated as the sum of the semi-empirical formula of Millikan and White (1963) obtained from the correlation between observed vibrational relaxation times over a temperature range of 300 K to 8000 K. The high temperature correction term proposed by Park (1989) is combined with the original formula of Millikan and White as follows:

$$\tau_{s,r} = p^{-1} \exp[A_{s,r}(T^{-1/3} - 0.015 B_{s,r}^{1/4}) - 18.42] + (N\sigma_v \sqrt{8RT/\pi M})^{-1},$$
$$B_{s,r} = M_s M_r / (M_s + M_r),$$
$$A_{s,r} = 1.16 \times 10^{-3} B_{s,r}^{0.5} \Xi_{vib,s}^{4/3},$$
$$\sigma_v = 10^{-17} (5 \times 10^4 / T)^2 \tag{9}$$

where N is the total number density, R is the universal gas constant, M is the average molecular weight, and $\Xi_{vib,s}$ is the characteristic temperature of molecular species s for vibration. The pressure p has to be used the unit of atm, and temperatures in K, the unit of the limiting cross section σ_v in cm, so that the vibrational relaxation times are obtained in sec.

Viscous model

The derivation of the transport coefficients such as the mixture viscosity μ, the frozen thermal conductivity η, the vibrational thermal conductivity η_v, and the effective diffusion coefficient of species s in the mixture D_s closely follows the approach proposed in (Lee, 1984). According to this approach, the coefficients are evaluated in terms of the molar concentration of species s, $\gamma_s = \rho_s/(\rho M_s)$, as follows:

$$\mu = \frac{M_s \gamma_s}{\gamma_r \Delta^{(2)}_{s,r}}, \eta = \eta_{tr} + \eta_{rot}, \eta_v = \eta_{rot}$$
$$D_s = \frac{\gamma_{tot}^2 M_s (1 - M_s \gamma_s)}{\gamma_r / D_{s,r} - \gamma_s / D_{s,s}}, D_{s,r} = \frac{RT}{p\Delta^{(1)}_{s,r}}, \gamma_{tot} = \sum_s \gamma_s \tag{10}$$

where M_s and R are the molecular weight of species s and universal gas constant, respectively.

The modified collision integrals $\Delta^{(1)}_{s,r}$ and $\Delta^{(2)}_{s,r}$ are in the following form,

$$\Delta^{(1)}_{s,r} = \frac{R\sigma^2_{s,r}\Omega_{s,r}}{\alpha\sqrt{T}} \sqrt{\frac{M_s M_r}{M_s + M_r}},$$
$$\Delta^{(2)}_{s,r} = \frac{\sqrt{M_s M_r}\,(\sqrt[4]{M_s \mu_r^2} + \sqrt[4]{M_r \mu_s^2})^2}{\mu_s \mu_r \sqrt{8(M_s + M_r)}} \tag{11}$$

where

$$\Omega_{s,r} = \left(\frac{T}{T^*_{s,r}}\right)^{-0.145} + \left(0.5 + \frac{T}{T^*_{s,r}}\right)^{-2}, \sigma_{s,r} = 0.5(\sigma_s + \sigma_r), T^*_{s,r} = \sqrt{T^*_r T^*_s} \tag{12}$$

In equation (12) the constant α, the effective temperature T^*_s, and the collision effective σ_s diameter can be found in White (1974).

The thermal conductivity coefficients of translational and rotational energy modes, η_{tr} and η_{rot} are given by

$$\eta_{tr} = 3.75R\frac{\gamma_s}{a_{s,r}\gamma_r \Delta^{(2)}_{s,r}}, \eta_{rot} = R\frac{\gamma_s \chi_s}{\gamma_r \Delta^{(1)}_{s,r}},$$
$$a_{s,r} = 1 + \frac{(1 - M_{s,r})(0.45 - 2.54 M_{s,r})}{(1 + M_{s,r})(1 + M_{s,r})}, M_{s,r} = \frac{M_s}{M_r} \tag{13}$$

where χ_s =0 for s=1,2, and χ_s =1 for s=3,4,5. Note that there are summations on repeating indexes r and s from 1 to 5 except for D_s, where the index r is the summation index only.

The single species viscosity μ_s can be estimated with the kinetic theory's formula of Chapman and Cowling (White, 1974) in the following form:

$$\mu_s = \frac{\beta\sqrt{M_s T}}{\sigma_s^2 \Omega_s}, \Omega_s = 1.147\left(\frac{T}{T_s^*}\right)^{-0.145} + \left(0.5 + \frac{T}{T_s^*}\right)^{-2} \tag{14}$$

where β is 2.6838×10^{-5}, the collision effective diameter σ_s and the effective temperature T_s^* are also given in White (1974).

Discrete equation

We use the finite volume method to obtain spatial discretization of the governing equations (1), where implicit time integration is performed for the inviscid and viscous flux vectors and the thermochemical source terms. The time integration by explicit methods is considerably time-consuming and not adequate for thermochemical nonequilibrium flows because of the extreme stiffness of the governing equations. The resulting system of discrete equations can be written as (Menshov and Nakamura, 1994):

$$\begin{aligned} &\omega_i \Delta\mathbf{q}_i + \Delta t \sum_\sigma s_\sigma \mathbf{f}_\sigma^{n+1} = \Delta t \sum_\sigma s_\sigma \mathbf{g}_\sigma^{n+1} + \omega_i \Delta t \mathbf{H}_i^{n+1}, \\ &\mathbf{f}_\sigma = \mathbf{f}_{k,\sigma} n_k, \mathbf{g}_\sigma = \mathbf{g}_{k,\sigma} n_k \end{aligned} \tag{15}$$

where $\mathbf{q}_i$ is the cell average solution vector, ω_i is the cell volume, S_σ is the area of the cell interface, and $\mathbf{n} = (n_1, n_2, n_3)$ is the exterior normal vector to the cell interface. Also the superscript n+1 and the subscript σ denote the time step and the cell interface, respectively, and Δt indicates the time increment. The summation is performed for all faces of the cell under consideration.

Introducing the local one-dimensional inviscid flux vector $\mathbf{F}$ and the transforming matrix T_σ, the inviscid numerical flux $\mathbf{f}_\sigma$ can be expressed in the following form:

$$\mathbf{f}_\sigma = T_\sigma^{-1}\mathbf{F}, \mathbf{F} = \mathbf{f}(\mathbf{Q}), \mathbf{Q} = T_\sigma \mathbf{q} \tag{16}$$

The flux vector $\mathbf{F}$ is defined by the values of the solution vector in the two cells adjacent to the cell interface, $\mathbf{F}=\mathbf{F}(\mathbf{Q}_i, \mathbf{Q}_{\sigma(i)})$, where σ_i is the number of the cell that adjoins the i-cell through the cell interface σ.

LU-SGS approximate factorization

To solve the system of discrete equation (15) we linearize the thermochemical source vector and approximate the inviscid local flux and the viscous flux in the following way:

$$\begin{aligned}\mathbf{H}_i^{n+1} &= \mathbf{H}_i^n + S_i \Delta \mathbf{q}_i, \\ \mathbf{F}^{n+1} &= \mathbf{F}^n + A_\sigma^{(1)} \Delta \mathbf{Q}_i + A_\sigma^{(2)} \Delta \mathbf{Q}_{\sigma(i)}, \\ \mathbf{g}_\sigma^{n+1} &= \mathbf{g}_\sigma^n + D_\sigma^{(2)} \Delta \mathbf{q}_{\sigma(i)} - D_\sigma^{(1)} \Delta \mathbf{q}_i\end{aligned} \tag{17}$$

where the matrices $A_\sigma^{(1)}$and $A_\sigma^{(2)}$, which are dependent on the solution vectors in adjoining cells, have to be consistent with the Jacobian matrix A of the flux **F** in the sense that

$$A_\sigma^{(1)}(\mathbf{Q},\mathbf{Q}) + A_\sigma^{(2)}(\mathbf{Q},\mathbf{Q}) = A(\mathbf{Q}) = \partial \mathbf{F} / \partial \mathbf{Q} \tag{18}$$

and $D_\sigma^{(1,2)}$ is a positive diagonal matrix with elements dependent on dissipative transport coefficients in the adjoining cells. It gives the system of equations in the Δ-form:

$$(I + \sum_\sigma \mu_\sigma^{(1)} - \Delta t S_i)\Delta \mathbf{q}_i + \sum_\sigma \mu_\sigma^{(2)} \Delta \mathbf{q}_{\sigma(i)} = \mathbf{R}_i \tag{19}$$

where S_i is the Jacobian matrix of the thermochemical source vector **H**, $\mu_\sigma^{(1)}$, $\mu_\sigma^{(2)}$, and $\boldsymbol{R}_i$ are given by

$$\begin{aligned}&\mu_\sigma^{(1)} = \frac{\Delta t}{\omega_i} s_\sigma (T_\sigma^{-1} A_\sigma^{(1)} T_\sigma + D_\sigma^{(1)} I), \mu_\sigma^{(2)} = \frac{\Delta t}{\omega_i} s_\sigma (T_\sigma^{-1} A_\sigma^{(2)} T_\sigma - D_\sigma^{(2)} I), \\ &\mathbf{R}_i = \Delta t \mathbf{H}_i^n + \frac{\Delta t}{\omega_i} \sum_\sigma s_\sigma (\mathbf{g}_\sigma^n - \mathbf{f}_\sigma^n)\end{aligned} \tag{20}$$

The second term on the left-hand side of equation (19) is expressed by,

$$\sum_\sigma \mu_\sigma^{(2)} \Delta \mathbf{q}_{\sigma(i)} = \sum\nolimits_L (\Delta \mathbf{q}) + \sum\nolimits_U (\Delta \mathbf{q}) \tag{21}$$

where

$$\begin{aligned}\sum\nolimits_L (\Delta \mathbf{q}) &= \sum_{\sigma:\sigma(i)<i} \mu_{\sigma(i)}^{(1)} \Delta \mathbf{q}_{\sigma(i)}, \\ \sum\nolimits_U (\Delta \mathbf{q}) &= \sum_{\sigma:\sigma(i)>i} \mu_{\sigma(i)}^{(2)} \Delta \mathbf{q}_{\sigma(i)}\end{aligned} \tag{22}$$

In order to solve the above system of discrete equations written in the Δ-form efficiently, it can be first approximately factorized by applying the Lower-Upper Symmetric Gauss-Seidel (LU-SGS) decomposition (Yoon and Jameson, 1988) and then solved by implementing forward and backward relaxation sweeps. For an arbitrary grid, this procedure can be generalized in the following way:

$$\begin{aligned}&(I + \sum_\sigma \mu_\sigma^{(1)} - \Delta t S_i)\Delta \mathbf{q}_i^* + \sum\nolimits_L (\Delta \mathbf{q}^*) = \mathbf{R}_i, \\ &(I + \sum_\sigma \mu_\sigma^{(1)})\Delta \mathbf{q}_i + \sum\nolimits_U (\Delta \mathbf{q}) = (I + \sum_\sigma \mu_\sigma^{(1)})\Delta \mathbf{q}_i^*\end{aligned} \tag{23}$$

where the intermediate values of the increment of solution vector $\Delta\mathbf{q}_i^*$ and it's final values $\Delta\mathbf{q}_i$ are calculated.

To provide the diagonal dominance property to these subsystems for stability of their solutions, the matrix splitting should be performed in such a way that $A_\sigma^{(1)}$ would be of positive eigenvalues and $A_\sigma^{(2)}$ would be of negative ones. We employ the simple way of splitting the Jacobian matrix, as proposed by Jameson and Turkel (1981), which guarantees the property mentioned above:

$$A_\sigma^{(1)} = A^+(\mathbf{Q}_i), A_\sigma^{(2)} = A^-(\mathbf{Q}_{\sigma(i)}), A^\pm = 0.5(A \pm \rho_A) \tag{24}$$

where ρ_A is the spectral radius of the Jacobian matrix A. A great interest of this splitting is that it results in a scalar form for the operator $\sum_\sigma \mu_\sigma^{(1)}$ where a regular grid is used.

The system of the above discrete equation (23) can be written in the standard Lower-Upper (LU) operator form as follows:

$$LD^{-1}U\Delta\mathbf{q} = \mathbf{R} \tag{25}$$

where

$$\begin{aligned} &L = D + \textstyle\sum_L(\Delta\mathbf{q}) - \Delta t S, U = D + \textstyle\sum_U(\Delta\mathbf{q}), \\ &D = I + \frac{\Delta t}{\omega}\sum_\sigma D_\sigma + \tilde{D}, \\ &\tilde{D} = \frac{\Delta t}{\omega}\sum_\sigma s_\sigma T_\sigma^{-1} A^+ T_\sigma \end{aligned} \tag{26}$$

Then the solution to equation (26) needs inversion of the operator D only.

Inviscid flux evaluation

To evaluate the inviscid numerical flux vector, consider the Advection Upstream Splitting Method (AUSM) (Liou and Steffen, 1993) extended to the system of equations under consideration (Menshov and Nakamura, 1994). The main advantage of this shock capturing scheme is that stationary contact discontinuity as well as shock waves can be captured with less numerical dissipation and robustness for strong discontinuities in hypersonic flows is superior to other shock capturing methods with approximate Riemann solver. The modification has been made only for the interface convective velocity definition. The velocity is computed by means of a symmetric averaging between the edge normal components of the velocity vectors in the cells adjoining to the edge. It allowed us to eliminate a slight numerical overshoot just behind the shock wave inherent to the AUSM.

Initial and boundary conditions

An impulsive start has been conducted for all calculations with or without an impinging shock. A zero pressure gradient ($\partial p/\partial n = 0$), constant temperature

($T=T_v=T_{wall}$), and no-slip conditions ($u=v=0$) are assumed at the body surface, where also a fully catalytic wall (FCW) conditions ($c_s = c_{s\infty}$) to finite-rate chemical reactions is considered. Here c_s ($=\rho_s/\rho$) denotes the mass concentration of chemical species s with $\Sigma_s c_s=1$, and the subscript ∞ means free-stream. At the outflow boundary, where the flow is assumed to be supersonic in the present calculation, the values are extrapolated from those at interior grid points. For the blunt body flow calculation, the values of free-stream are fixed at the inflow boundary, while for shock-on-shock interference cases free-stream conditions are imposed at the points on the inflow boundary above the impinging point of an oblique shock. In the latter the values obtained from shock jump relations (frozen-flow Rankine-Hugoniot relationship) for the given flow Mach number and impinging shock angle are specified to the post-shock points on the inflow boundary. The chemical reactions and the vibrational relaxation, therefore, are assumed to be frozen across the impinging weak oblique shock wave.

Numerical results and discussion

Heat flux on blunt body in hypersonic flows

Using the above described numerical methods and physical models, the Navier-Stokes equations for a multi-component reacting gas with vibrational relaxation have been solved for the type-IV shock-on-shock interaction and simple blunt body flows. First of all, the high-enthalpy flowfields with strong thermochemical nonequilibrium effects reported previously in literatures have been simulated to validate the accuracy of the present numerical code. Specifically, hypersonic nitrogen and air flows around blunt bodies were calculated for the comparison with the results of Hornung's and Lobb's experiments.

In Figure 2 (a), the numerical interferogram constructed from the calculated density distribution is compared with the experimental one of Hornung (1972) who obtained interferograms with infinite fringes in the two-dimensional nitrogen flow produced by a free-piston driven shock tunnel. The free-stream conditions for this case are as follows: $\rho_\infty=5.35\times10^{-3}$ kg/m^3, $u_\infty=5.59$ km/s, $T_\infty=T_{v\infty}=1833$ K, $c_{N2}=0.93$, $c_N=0.07$. The free-stream gas is pure nitrogen and the diameter of the circular cylinder D_b is 5.08 cm. The frozen-flow Mach number M_∞ is 6.13 and the Reynolds number ($Re_\infty=\rho_\infty u_\infty D_b/\mu_\infty$) based on the body diameter is about 2×10^4. A 40×60 node mesh system was used in the numerical calculation. The numerical calculation for nitrogen flow, using the present code for five-species two-temperature air flow, was conducted by setting the mass concentrations of the other species to zero. The strong nonequilibrium chemical process and vibrational relaxation occur following the bow shock in the stagnation region of the flow. By comparing the numerical and experimental interferograms, it is readily apparent that the present code accurately reproduces the general structure of the nonequilibrium high-enthalpy flowfield. The comparison of both results show good agreement in both shock shape and fringe patterns, though the slight discrepancy of the fringe patterns in the stagnation region is observed. The shock stand-off

distance predicted by the present numerical code is also compared with a ballistic range experiment of Lobb (1964) for the nonequilibrium air flow over a sphere with a radius of 6.65 mm. The numerically calculated isobars and experimental shadowgraph are shown in Figure 2 (b). The free-stream conditions are $\rho_\infty = 7.8 \times 10^{-3}$ kg/m^3, $u_\infty = 5.28$ km/s, $T_\infty = T_{v\infty} = 273$ K, $c_N = c_O = c_{NO} = 0$, $c_{N2} = 0.765$, $c_{O2} = 0.235$, and the frozen Mach number is 15.3. It can be shown that the present code successfully reproduces the shock shape and shock stand-off distance in a hypersonic air flow in a thermochemical nonequilibrium regime from the comparison in Figure 2(b).

For the quantitative comparison with experimental data, heat flux calculations on blunt body surface have been performed for the hypersonic flow around spheres. The calculation simulates the recent experiment (Hanamitsu *et al.,* 1996) using a high-enthalpy shock tunnel (HEG) in DLR, Germany. The free-stream conditions of the experiments are, $\rho_\infty = 1.56 \times 10^{-3}$ kg/m^3, $u_\infty = 5.94$ km/s, $T_\infty = T_{v\infty} = 705$ K, $c_{N2} = 0.762$, $c_{O2} = 0.0348$, $c_{NO} = 0.0317$, $c_O = 0.1708$, $c_N = 0$. The corresponding total enthalpy and total temperature are $H_0 = 21.06$ MJ/kg and $T_0 = 9055$ K, respectively. The flow Mach number is 11.2 and the Reynolds number based on the free-stream values and the sphere diameter ($D_b = 4$ cm) is 1.14×10^4. In this experiment, the convective heat transfer rates along the

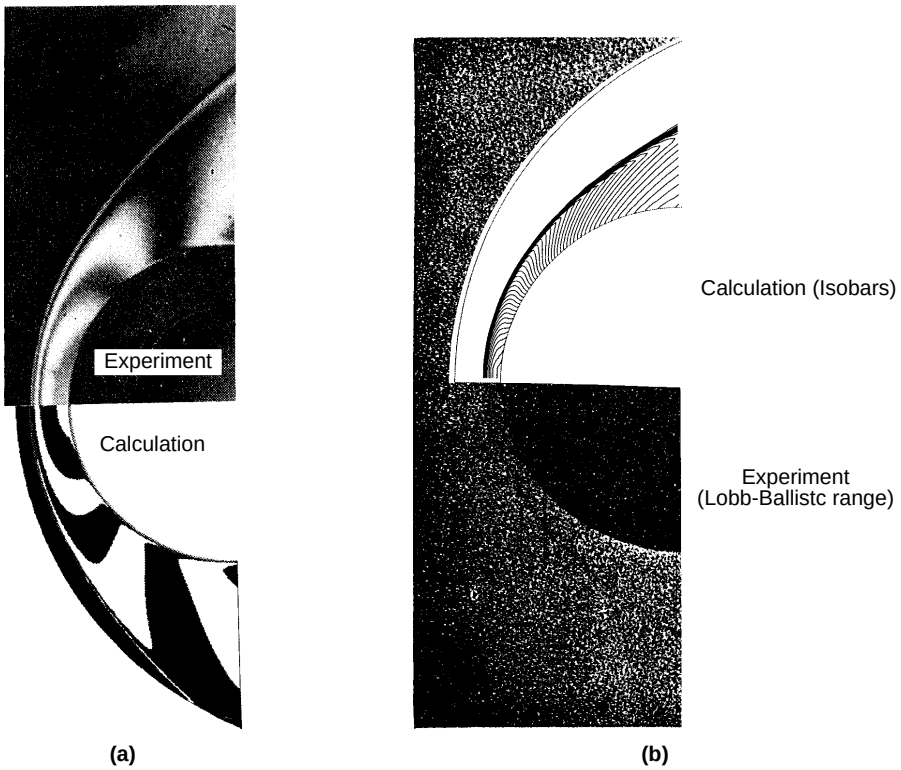

Figure 2. Comparison of numerical and experimental results: (a) numerical and experimental interferograms for a nonequilibrium nitrogen flow around a cylinder; (b) numerical isobars and shadowgraph for a hypersonic projectile in air

sphere surface were measured under various free-stream conditions. A non-uniform grid consisting of 60 cells in the radial direction and 30 cells in the direction along the sphere is clustered in the boundary layer and characterized by a minimum cell size at the sphere wall Δy_{min}. The total heat flux is calculated by the summation of three contribution parts, i.e., translational/rotational temperature mode flux, vibrational/electronic temperature mode flux and diffusion mode flux as follows:

$$\dot{q}_{total} = \eta \frac{\partial T}{\partial n} + \eta_v \frac{\partial T_v}{\partial n} + \sum_{s=1}^{N} \rho h_s D_s \frac{\partial y_s}{\partial n} \tag{27}$$

The calculated $\dot{q}_{total}$ distributions on blunt body surface are shown in Figure 3, where the experimental values are also given as a symbol of solid square. The calculated and measured heat fluxes at stagnation point show very reasonable agreement. The deviation between the numerical and experimental values at θ=20 deg, however, is found. The reason for this peak heating in downstream region observed in the DLR experiment (Hanamitsu *et al.,* 1996) is not made clear so far. The stagnation point heat flux predicted from the well-known Fay-Riddel theory is also given as F-R in the figure. The theoretically predicted value (F-R) is lower than the numerical and experimental ones, the value of which is about 70 per cent of measurement. The Fay-Riddel theory also underestimates the stagnation point heat flux for other cases, which are not given here. In addition, the heat fluxes predicted under non-catalytic wall

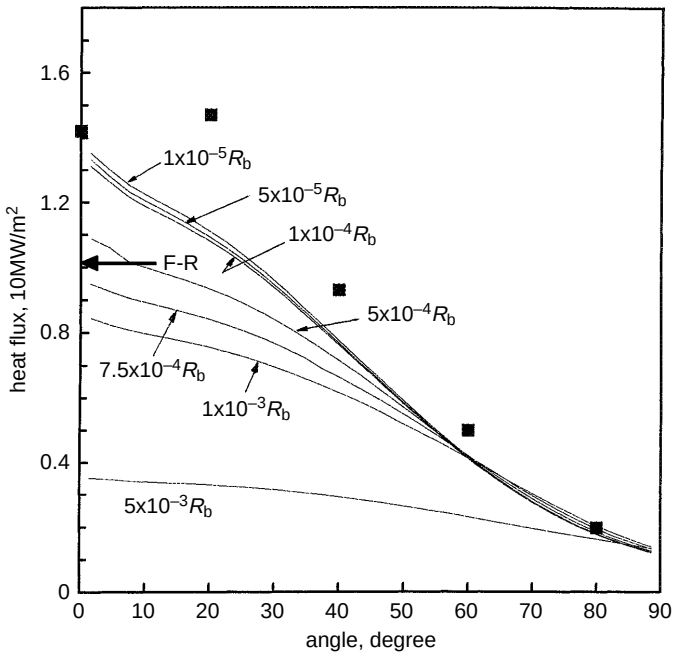

Figure 3.
Mesh Reynolds number effect on heat flux evaluation

(NCW) boundary conditions ($\partial c_s/\partial n=0$) are much deviated from the experimental data than those with fully catalytic wall (FCW) conditions ($c_s=c_{s\infty}$). The heat flux value at stagnation point, predicted with NCW boundary conditions for this case, is about half of the experimental value.

Klopfer and Yee (1988) showed that the numerically predicted heat flux value is crucially dependent on the cell size on the body surface from their calorically perfect gas calculations. We also investigated grid convergence on heat flux prediction for the present thermochemical nonequilibrium case. The results shown in the figure indicate that the grid size spacing in boundary layer turns out to be of great importance for accurate heat flux calculations. Even a small value of order 10 of the cell Reynolds number ($Re_{cell} = Re_\infty \Delta y_w/D_b$) might result in 100 per cent error in the vicinity of the stagnation point. It should be noted that minimum cell size of $1 \times 10^{-4} R_b$ at the body surface is required for the accurate prediction of nonequilibrium heat flux. However, the results show that the heat flux distribution over θ=55 deg is free from the cell Reynolds number effect.

The contribution of each heat flux mode to the total heat flux is shown in Figure 4. The contribution of the convective heat flux in the vibrational/electronic mode is less than 10 per cent of the total heat flux. The translational/rotational heat flux is dominant, the value of which is about 70 per cent of the total heat flux.

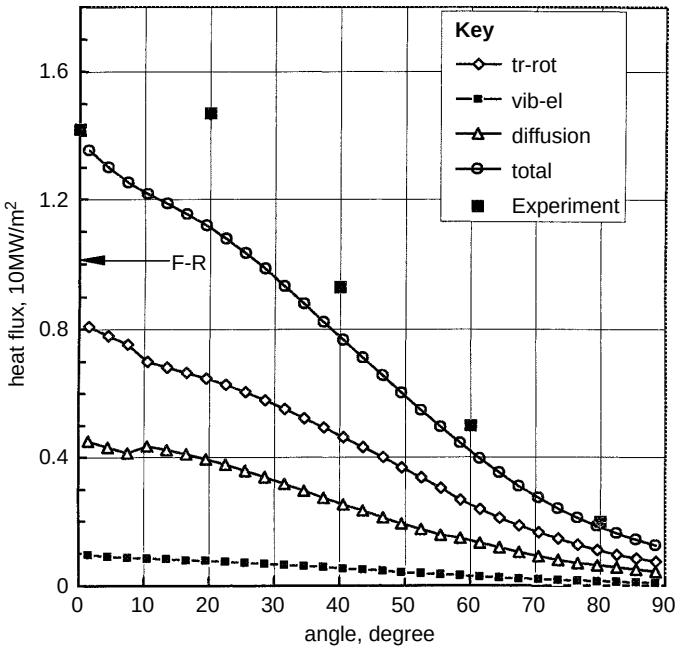

Figure 4.
Contribution of each mode to total heat flux

Heat flux in shock-on-shock interaction flowfield

The numerical results for the type-IV shock-on-shock interaction flowfield are shown as contours of flow and thermal properties and close-up of velocity vectors in Figures 5 and 6, respectively. The free-stream conditions are $\rho_\infty = 7.8 \times 10^{-3}$ kg/m^3, $u_\infty = 5.28$ km/s, $T_\infty = T_{v\infty} = 273$ K, $c_N = c_O = c_{NO} = 0$, $c_{N2} = 0.765$, $c_{O2} = 0.235$. The impinging angle of an oblique shock wave is 25 deg and the curvature radius of a cylindrical body is $R_b = 3$ cm. The body surface is assumed to be fully catalytic wall (FCW). The grid number used in the calculation is 120×240. It was found from the results for blunt body flows that at least Δy_w of $1 \times 10^{-4} R_b$ in the direction normal to the body was necessary. Hence, the cell size on the body surface Δy_w is set to be $1 \times 10^{-4} R_b$.

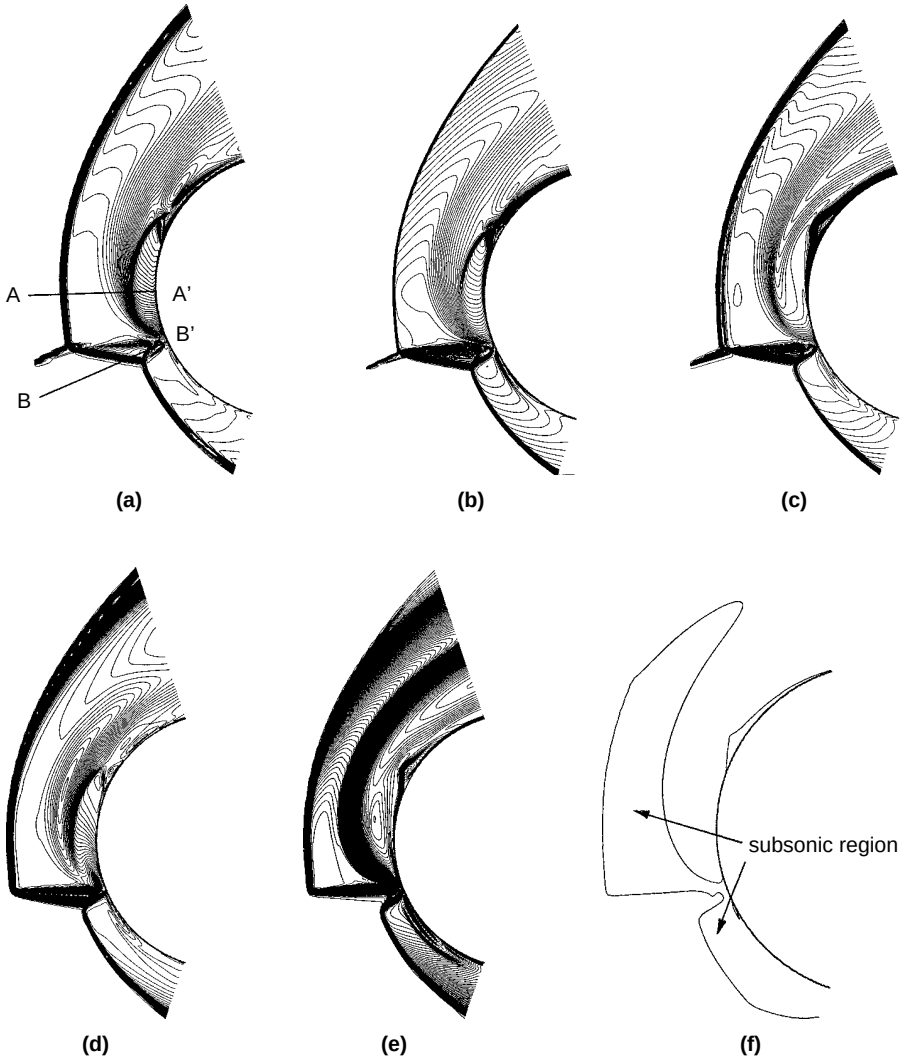

Figure 5.
Calculated results of nonequilibrium type-IV shock-on-shock interaction flowfield: (a) translational/rotational temperature contours; (b) Mach number contours; (c) N_2 density contours; (d) NO density contours; (e) N density contours; (f) sonic line showing subsonic region

As can be seen from the figures, the shear layers develop from the two triple points and the supersonic jet between the shear layers is formed. Also it can be observed from the close-up of velocity vectors in Figure 6 that the supersonic jet embedded in the type-IV shock-on-shock interaction flowfield impinges to the wall surface in nearly normal direction, where high- pressure region with a distinct peak point is generated. Kortz *et al.* (1995) reported that the supersonic jet and peak heat flux were not observed under their experimental conditions. They explained that the reason for that could be the total pressure loss due to endothermic chemical reactions behind a strong shock wave in a nitrogen flow. However, the present and DSMC (Carlson and Wilmoth, 1994) results clearly show the supersonic jet structure embedded in the type-IV shock-on-shock interaction flowfield that plays an important role in aerodynamic heating enhancement on the body surface. It should be mentioned that the flow conditions for three cases are not same. For comparison, a calorically perfect gas case has also been calculated, the result of which is shown as isotherms in Figure 7. The flow conditions are same to nonequilibrium case. From this result, it can be observed that the shock stand-off distance of the perfect gas case is larger than that of the thermochemical nonequilibrium case as expected. In addition, the maximum heat flux predicted by the perfect gas calculation is two times larger than that of nonequilibrium case, and the maximum post-shock frozen state temperature is about 18,800 K. However the peak pressure on body surface predicted by the perfect gas calculation shows nearly same value with nonequilibrium case. In general, it is well known that pressure distribution is not sensitive to chemical reaction and/or excitation of internal energy modes in hypersonic high-enthalpy flow. The present numerical results also reveal similar feature in pressure prediction in high-enthalpy flow.

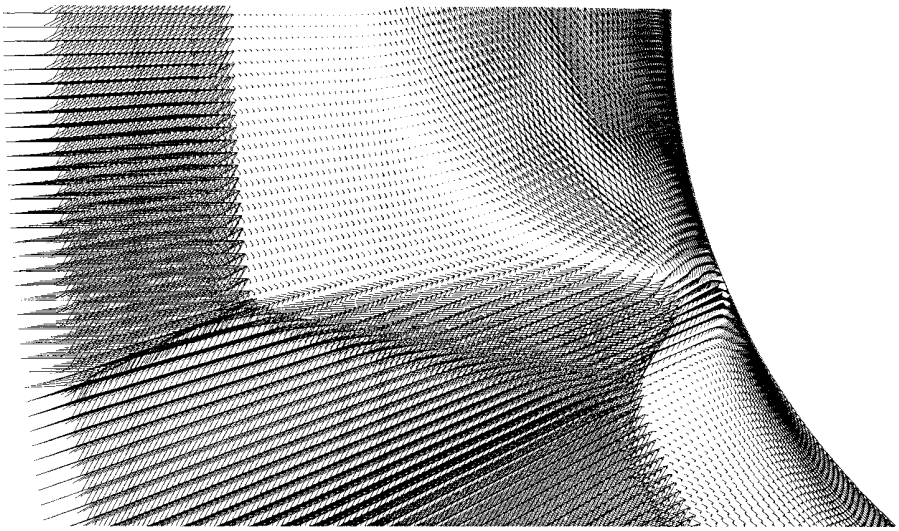

Figure 6.
Close-up of velocity vectors for type-IV shock-on-shock interaction flowfield

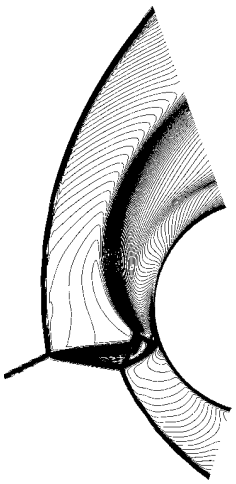

Figure 7.
Structure of type-IV shock-on-shock interaction flowfield with calorically perfect gas of air; temperature contours

The static pressure distribution on body surface is shown in Figure 8. The local maximum pressure is 11 times larger than the reference value of the case without shock-on-shock interaction. The heat flux distribution along the cylindrical body surface is shown in Figure 9, and the peak value of heat transfer rate is about ten times larger than the reference value. Though the maximum values of translational/rotational and vibrational/electronic heat fluxes are found at the same location, the peak location of diffusive heat flux is

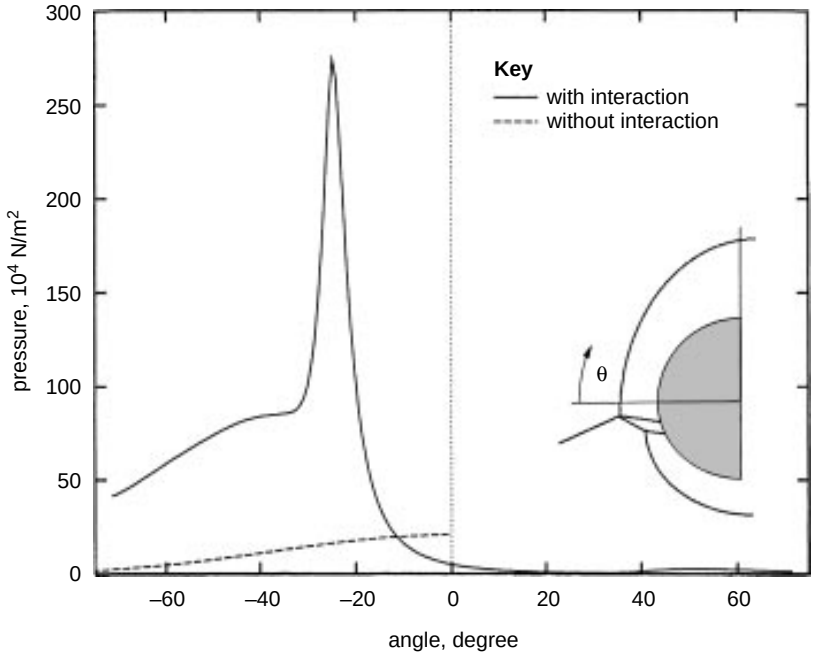

Figure 8.
Static pressure distribution along the body surface

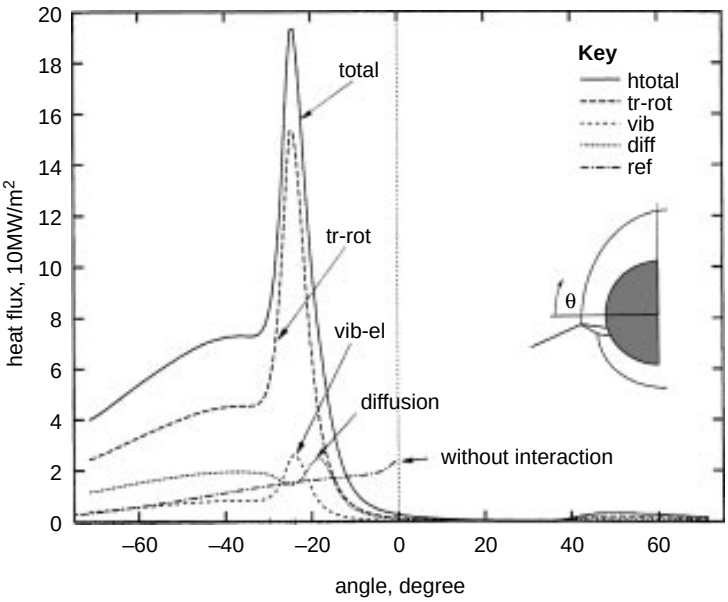

Figure 9.
Heat flux distribution along the body surface

deviated from the abovementioned two modes. The total heat flux is mainly contributed by the translational/rotational flux, the value of which is about 80 per cent. The contribution due to the convective heat flux in the vibrational/electronic mode is found to be in the same order with that in the diffusion mode.

Figures 10 and 11 show the profiles of temperature and mass concentration of chemical species, respectively, along $\theta=0$ line (cut A-A′). The thermal

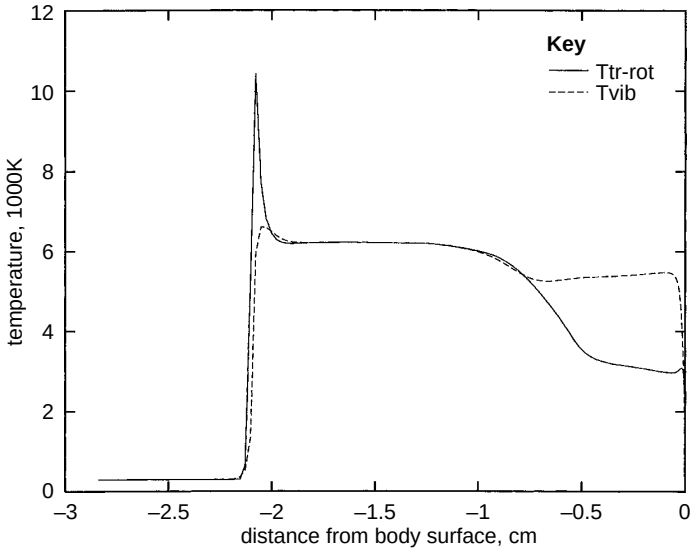

Figure 10.
Temperature profile on θ=0 (cut A-A′)

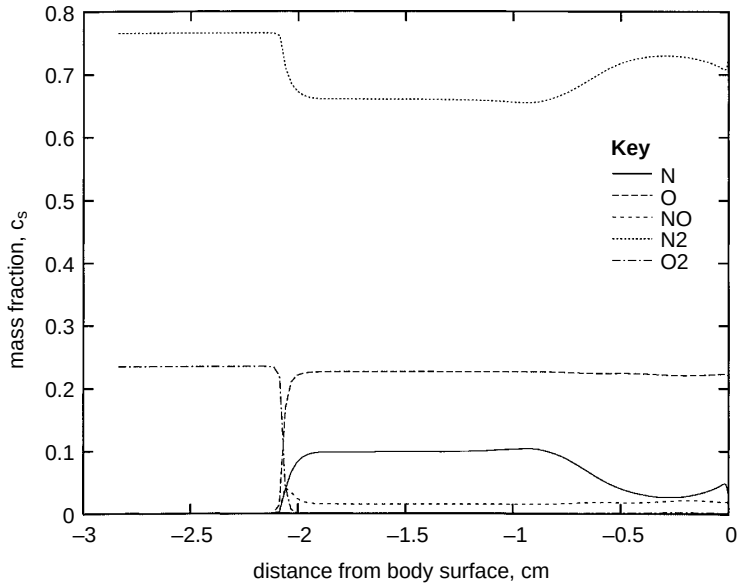

Figure 11.
Mass concentration profile of each species on θ=0 line

nonequilibrium relaxation length behind the upper portion of a bow shock wave is about 0.2 cm and the maximum temperature behind the bow shock increases as high as 11,000K. It can be seen from the temperature profile that there is a thermal nonequilibrium ($T \neq T_v$) region in the vicinity of the body surface, where the vibrational temperature deviates from its equilibrium value with the translational temperature. This region corresponds to the supersonic expanding region of a wall jet near the body surface. In this expanding region, mass concentration of N decreases because of recombination reaction due to sudden expansion from high-pressure stagnation region where the embedded supersonic jet impinges. As a result of recombination reaction, contrariwisely, the N_2 concentration increases. However the O_2 molecules, easily dissociating at relatively low temperature compared with N_2 molecule, are fully dissociated behind the strong bow shock and its mass concentration is nearly not changed across the supersonic expanding region near the body surface. The distribution of both translational and vibrational temperatures is shown in Figure 12, which is along cut B-B′ depicted in Figure 5 (a). It can be found that the thermal nonequilibrium effects are prevalent inside the embedded supersonic jet structure, and that the two internal energy modes described by T and T_v reach nearly equilibrium state ($T \approx T_v$) at the location of terminating jet bow shock.

The inherent unsteadiness of type-IV shock-on-shock interaction flowfield was reported previously by perfect gas calculations (Gaitonde and Shang, 1995; Lind, 1997; Zhong, 1994;) and experiment (Holden, 1990). Gaitonde and Shang (1995) obtained a dominant frequency of about 32 kHz for oscillation. On the other hand, the experimental observation by Holden (1990) showed that the frequencies for type-IV interactions are in the range of 3~10 kHz. The

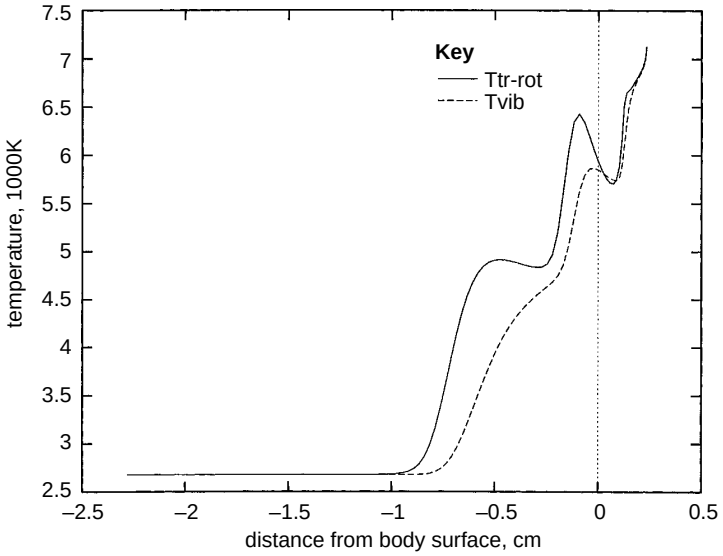

Figure 12.
Temperature profile along cut B-B′

mechanism of the unsteadiness, however, has not been sufficiently clarified, although some possible reasons have been proposed. The pressure wave, generated by the interaction between the shock waves in the supersonic jet structure and the shear layer outside the jet, propagates to the upstream direction, and the shear layer itself has Kelvin-Helmhortz instability. These disturbances propagate to the upstream through the subsonic shock layer (inside sonic line in Figure 5 (f)), which makes the bow shock wave oscillate. The present numerical results also indicate the unsteady motion of a bow shock wave, i.e., the stand-off distance keeps changing continuously. In the present calculation, the subsonic region on the upper side is larger than the lower one, where strong oscillation of bow shock was observed. It can be seen in Figure 5 (f) that a supersonic region exists between the subsonic region and the body surface in the upper region, where it flows along the cylindrical body surface after impinging the body. The surface pressure fluctuation at $\theta = 0$ deg is shown in Figure 13. The FFT (Fast Fourier Transformation) analysis for the fluctuating surface static pressure at $\theta = 0$ deg gives the dominant fluctuation frequency of about 30 kHz in this calculation, which frequency value is close to that of Gaitonde and Shang (1995).

Concluding remarks

The numerical calculations have been conducted for the purpose of predicting convective heat transfer rates to the body surface in hypersonic flows in a thermochemical nonequilibrium regime. The Navier-Stokes equations for a chemical reacting and vibrational relaxing high-temperature gas mixture have been solved by AUSM and LU-SGS methods. Numerical results are compared with some experiments using hypersonic impulse facilities, where

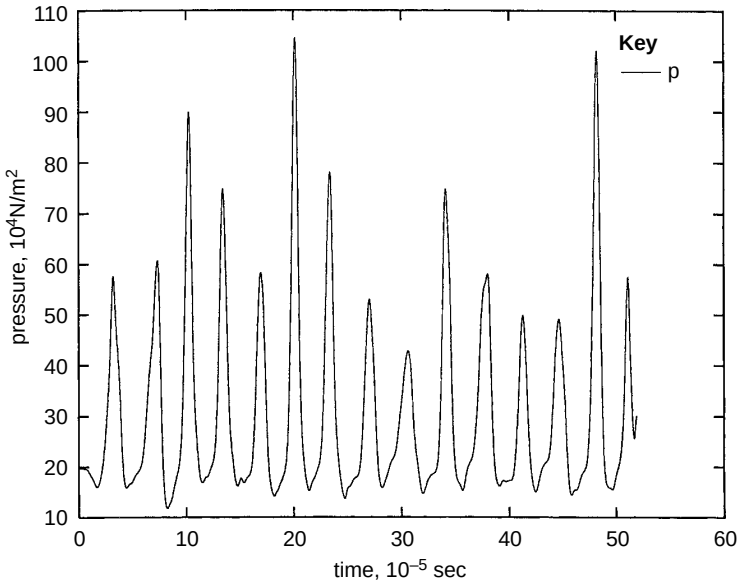

Figure 13.
Time variation of surface pressure at θ=0

satisfactory quantitative and qualitative agreements are obtained in terms of shock wave shape, shock stand-off distance, and convective heat transfer rate on body surface.

A hypersonic type-IV shock-on-shock interaction flowfield is investigated to see complicated flow phenomena with thermochemical nonequilibrium effects. The heat flux in nonequilibrium blunt body flow with an oblique impinging shock wave is extremely enhanced because of the impingement of a supersonic jet generated from the type-IV shock-on-shock interaction. The local maximum pressure and heat flux are about ten times larger than those without shock-on-shock interaction. The numerical results also show that the contribution of the translational/rotational heat flux to total heat transfer rate is dominant. In addition, it is worth mentioning that strong nonequilibrium phenomena occur inside both the supersonic impinging jet embedded in the type-IV interaction flowfield and expanding wall jet near the body surface. Furthermore, it is also found that the interacting bow shock wave moves unsteadily in the high-enthalpy flowfield with a dominant fluctuation frequency of 30 kHz.

References

Bruck, S. (1997), "Investigation of shock-shock interactions in hypersonic reentry flows", *Proc. of 20th Inter. Symp. on Shock Waves,* Scientific Publishing Co., pp. 209-14.

Carlson, A.B. and Wilmoth, R.G. (1994), "Monte Carlo simulation of a near-continuum shock-shock interaction problem", *J. Spacecraft & Rockets,* Vol. 31, pp. 25-30.

Edney, B. (1968), *Anomalous Heat Transfer and Pressure Distributions on Blunt Bodies at Hypersonic Speed in the Presence of an Impinging Shock,* Report 115, Aeronautical Research Inst., Federal Aviation Administration, Sweden.

Gaitonde, D. and Shang, J.S. (1995), "On the structure of an unsteady type IV interaction at Mach 8", *Computers & Fluids,* Vol. 24, pp. 469-85.

Hanamitsu, A., Kishimoto, T, and Bito, H. (1996), *High Enthalpy Flow Computation and Experiment Around the Simple Bodies,* Special Publication of National Aerospace Laboratory, SP-29, Japan, pp. 10-16.

Holden, M.S. (1990), "Shock-shock boundary layer interactions", AGARD Report 764, Special Course on Three-Dimensional Supersonic/Hypersonic Flows including Separation.

Holden, M.S., Moselle, J.R. and Lee, J. (1992), "Studies of aerothermal loads generated in regions of shock/shock interaction in hypersonic flow", NASA, CR-181893.

Hornung, H.G. (1972), "Nonequilibrium dissociating nitrogen flow over spheres and circular cylinders", *J. Fluid Mech.,* Vol. 53, pp. 149-76.

Jameson, A. and Turkel, E. (1981), "Implicit schemes and LU decompositions", *Math. of Comp.,* Vol. 37, pp. 385-97.

Klopfer, G.H. and Yee, H.C. (1988), "Viscous hypersonic shock-on-shock interaction on blunt cowl lips", AIAA Paper 88-0233.

Kortz, S., McIntyre, T.J. and Eitelberg, G. (1995), "Experimental investigation of shock-on-shock interactions in high-enthalpy shock tunnel Gottingen (HEG)", *Proc. of 19th Inter. Symp. on Shock Waves,* Springer, pp. 75-80.

Lee, J-H. (1984), "Basic governing equations for the flight regimes of aeroassisted orbital transfer vehicles", *Prog. Astr. Aeron.,* Vol. 96, pp. 3-54.

Lind, A. (1997), "Effect of geometry on the unsteady type-IV shock interaction", *J. Aircraft,* Vol. 34, pp. 64-71.

Liou, M-S. and Steffen, C.J. (1993), "A new flux splitting scheme", *J. Comp. Phys.,* Vol. 107, pp. 23-9.

Lobb, R.K. (1964), "Experimental measurement of shock detachment distance on spheres", in Nelson, W.C. (Ed.), *The High Temperature Aspects of Hypersonic Flow,* Pergammon, New York, NY, pp. 519-27.

Menshov, I. and Nakamura, Y. (1994), "Implementation of the LU-SGS method for an arbitrary finite volume discretization", *Proc. of 6th Japanese CFD Symp.,* Tokyo, pp. 123-24.

Millikan, R.C. and White, D.R. (1963), "Systematic of vibrational relaxation", *J. Chem. Phys.,* Vol. 39, pp. 3029-213.

Park, C. (1989), *Nonequilibrium Hypersonic Aerothermodynamics,* Wiley, New York, NY.

Tannehill, J.C., Holst, T.L. and Rakich, J.V. (1976), "Numerical computation of two-dimensional viscous blunt flows with an impinging shock", *AIAA J.,* Vol. 14, pp. 204-11.

Thareja, R.R., Stewart, J.R., Hassan, O., Morgan, K. and Peraire, J. (1989), "A point implicit unstructured grid solver for the Navier-Stokes equations", *Int. J. Numer. Methods Fluids,* Vol. 9, pp. 405-25.

Vincenti, W.G. and Kruger, C.H. (1993), *Introduction to Physical Gas Dynamics,* Krieger Publishing Co., pp. 197-245.

White, F.M. (1974), *Viscous Fluid Flow,* McGraw-Hill Co., pp. 27-36.

Yoon, S. and Jameson, A. (1988), "Lower-Upper method for the Euler and Navier-Stokes equations", *AIAA J.,* Vol. 26, pp. 1025-26.

Zhong, X. (1994), "Application of essentially nonoscillatory schemes to unsteady hypersonic shock-shock interference heating problems", *AIAA J.,* Vol. 32, pp. 1606-16.